Earth, Planets and Space

Open Access

Geometric correction for thermographic images of asteroid 162173 Ryugu by TIR (thermal infrared imager) onboard Hayabusa2

Takehiko Arai[1,2]*, Tatsuaki Okada[3,4], Satoshi Tanaka[4,5], Tetsuya Fukuhara[6], Hirohide Demura[7], Toru Kouyama[8], Naoya Sakatani[6], Yuri Shimaki[3], Hiroki Senshu[9], Tomohiko Sekiguchi[10], Jun Takita[11], Naru Hirata[7] and Yukio Yamamoto[3]

Abstract

The thermal infrared imager (TIR) onboard the Hayabusa2 spacecraft performed thermographic observations of the asteroid 162173 Ryugu (1999 JU$_3$) from June 2018 to November 2019. Our previous reports revealed that the surface of Ryugu was globally filled with porous materials and had high surface roughness. These results were derived from making the observed temperature maps of TIR using a projection method onto the shape model of Ryugu as geometric corrections. The pointing directions of TIR were calculated using an interpolation of data from the SPICE kernels (NASA/NAIF) during the periods when the optical navigation camera (ONC) and the light detection and ranging (LIDAR) observations were performed. However, the mapping accuracy of the observed TIR images was degraded when the ONC and LIDAR were not performed with TIR. Also, the orbital and attitudinal fluctuations of Hayabusa2 increased the error of the temperature maps. In this paper, to solve the temperature image mapping problems, we improved the correction method by fitting all of the observed TIR images with the surface coordinate addressed on the high-definition shape model of Ryugu (SFM 800k v20180804). This correction adjusted the pointing direction of TIR by rotating the TIR frame relative to the Hayabusa2 frame using a least squares fit. As a result, the temperature maps spatially spreading areas were converged within high-resolved 0.5° by 0.5° maps. The estimated thermal inertia, for instance, was approximately 300~350 Jm^{-2}s$^{-0.5}$K^{-1} at the hot area of the Ejima Saxum. This estimation was succeeded in case that the surface topographic features were larger than the pixel scale of TIR. However, the thermal inertia estimation of smooth terrains, such as the Urashima crater, was difficult because of surface roughness effects, where roughness was probably much smaller than the pixel scale of TIR.

Keywords: Hayabysa2, Asteroid, Ryugu, Thermal infrared imager, TIR, Shape model, Thermal model, Surface roughness

Introduction

Hayabusa2 is a Japanese asteroid sample return mission that rendezvoused with the asteroid 162173 Ryugu (previously known as 1999 JU$_3$) from June 2018 to November 2019 (Tsuda et al. 2013). Ryugu is classified as a C-type asteroid (Binzel et al. 2004), which is considered a parent body of carbonaceous chondrites. Based on the ground and space telescopic observations of Ryugu before the arrival of the Hayabusa2, its rotation period was found to be 7.63 h, and the thermal inertia was estimated to be 150~300 Jm^{-2}s$^{-0.5}$K^{-1} (Müller et al. 2017).

After the arrival of Hayabus2, the observation using the near-infrared spectrometer, NIRS3, suggested that the surface materials of Ryugu are similar to thermally or shock-metamorphosed carbonaceous chondrites

*Correspondence: araitakehiko@maebashi-it.ac.jp
[1] Division of Systems and Information Engineering, Ashikaga University, Ashikaga 326-8558, Japan
Full list of author information is available at the end of the article

Arai *et al. Earth, Planets and Space*   (2021) 73:115

Page 2 of 11

(Kitazato et al. 2019). The optical navigation camera, ONC, found several characteristic features of the surface on the scale of centimeters to meters; they are large ridges, regolith deposits, and cracked rocks (Sugita et al. 2019). The gravitational observation indicated that the bulk density of Ryugu is 1.19 ± 0.02 gcm^{-3} (Watanabe et al. 2019). The thermal infrared imager, TIR, suggested that the surface of Ryugu is filled with porous materials derived by the thermal inertia estimation (Okada et al. 2020). These results implied that Ryugu is composed of coalesced rubble piles.

TIR onboard Hayabusa2 is a thermographic camera with 328×248 pixels resolution (Okada et al. 2017). Its sensor is an array of microbolometers, and one pixel has a size of 37 μm. The observation wavelength is integration energy ranges from 8 to 12 μm. The field of view is an angle of $16.74° \times 12.66°$, and the spatial resolution is 0.051°/pixel. The goal of TIR is to reveal the thermophysical states of the Ryugu surface, such as grain size and/or its porosity (e.g. Grott et al. 2020), which affects the orbit of the asteroid due to radiation force (Yarkovsky effect, e.g., Bottke et al. 2006). The thermophysical state is usually characterized by thermal inertia, which is written as $\Gamma = \sqrt{\rho c_p k}$, where ρ is the bulk density, k is the thermal conductivity, and c_p is the specific heat.

Okada et al. (2020) estimated the global thermal inertia of Ryugu by comparing the calculation results of a thermophysical model, TPM-1 (Takita et al. 2017), with the observed images on 1 August 2018 (the mid-altitude observation; hereafter Mid-Alt observation). TPM-1 utilized a shape model of Ryugu with 196,608 polygons (SFM 200k v20180804, Watanabe et al. 2019) whose polygon size was comparable to the pixel scale of TIR in the Mid-Alt observation ($\sim$5 m / pixel). TPM-1 anticipated the surface temperature by calculating incident solar flux for all polygons, including secondary radiations and solar ray scatterings from surrounding polygons. The resulting global thermal inertia of Ryugu was roughly estimated to be 300 $\pm$ 100 Jm^{-2}s$^{-0.5}$K^{-1}. Nevertheless, TPM-1 could not reproduce the observed temperature distribution of Ryugu; it generated higher temperature than the observed TIR images around the sub-solar region of Ryugu and lower temperature at the dawn and dusk regions ($\sim$asteroid limb). The observed TIR images were broadly homogeneous over the hemisphere (e.g., Fig. 2 in Okada et al. 2020). This phenomenon is considered to be caused by surface roughness within a spatial resolution of the sensor (e.g. Groussin et al. 2007).

Shimaki et al. (2020) evaluated temperature profiles by using a thermophysical model that utilized a local rough surface model, TPM-2, which successfully reproduced the observed temperature profiles of Ryugu. TPM-2 simulates solar incident flux and thermal radiation from a local rough surface, which corresponds to be smaller than the spatial resolution of TIR. The temperature profiles of the local areas were obtained by projecting observed brightness temperature images for one asteroid rotation onto each polygon face of the shape model of Ryugu. By comparing the calculated and observed temperature profiles, the thermal inertia and surface roughness were derived; the mean value was estimated to be 225 $\pm$ 45 Jm^{-2}s$^{-0.5}$K^{-1} with the mean RMS slope of 47 $\pm$ 5°. TPM-2 produces only local temperature variation using the surface roughness model smaller than the pixel scale of TIR. Therefore, temperature profiles do not depend on the topographic shape of Ryugu, such as shadowing by large boulders (e.g. Ejima Saxum, Fig. 12 in Shimaki et al. 2020).

The quality of the observed temperature profiles, which depends on the accuracy of the image mapping onto a shape model, is important for comparing the observed and calculation results. The mapping was carried out using the numerical geometry tool kit, SPICE kernels (NASA/NAIF). It includes spacecraft attitudes, spacecraft altitudes, and the TIR alignment. The attitudes and altitudes were derived from data of the orbit control system (AOCS), ONC images, and measured altitudes by LIDAR. The pointing directions of TIR were calculated using interpolation of the data from SPICE kernels during the periods when the ONC or LIDAR observation was performed. However, the mapping accuracy of the observed TIR images was degraded when the ONC and LIDAR observations were not performed together with TIR. Also, the orbital and attitudinal fluctuations of Hayabusa2 increased the error of temperature maps.

The TIR alignment is defined by the TIR frame relative to the Hayabusa2 frame as Euler angles. The alignment was firstly determined in the Moon observation (Moon distance >763,000 km) during the Earth swingby (Okada et al. 2018); the resulting Euler angle was $(\theta_z, \theta_y, \theta_x) = (-1.077°, -180.080°, 0.141°)$ (hyb2_v09. tf, SPICE kernel). This Euler angle was a specific value obtained from the point source observation. We updated the alignment of TIR just after the arrival of Hayabusa2 using the observation data of Mid-Alt observation (Okada et al. 2020; Shimaki et al. 2020); the resulting value was $(\theta_z, \theta_y, \theta_x) = (-1.052°, -180.007°, 0.115°)$ (hyb2_v14.tf, SPICE kernel). This Euler angle was the mean value determined by using the same method of geometric correction in this study. However, we found that the value of θ_z, the rotation angle of the TIR boresight, has a bimodal path in the clockwise and the counterclockwise rotations. This value was specific and inadequate for other observation data. Therefore, determining the precise alignment and pointing directions are required for improving the image mapping of TIR.

Arai *et al. Earth, Planets and Space*   (2021) 73:115

Page 3 of 11

In this paper, to improve the mapping quality of observed images of TIR, we developed a geometric correction method by performing a one-to-one correspondence between the observed points in the TIR images and the surface coordinate addressed on the high-definition shape model of Ryugu. We show the corrected projection maps and discuss the temperature and thermal inertia estimations, which depend on the topographic variation of the Ryugu surface.

Data

We adapted a geometric correction for all TIR images observed in the early major observations period (Box-A on 2018-07-10, Box-C on 2018-07-20, Mid-Alt on 2018-08-01, and Box-B on 2018-08-31). The nominal observations of Hayabusa2 were called Box-A, -B, and -C (Watanabe et al. 2019). The Box-A (Home Position) was performed at an altitude of around 20 km at the sub-Earth point. The Box-B was performed at an altitude of 20 km, moving the horizontal direction within 9 km. The Box-C was performed at a low altitude below 20 km at the sub-Earth point. Besides the Box observations, several observations were carried out at low altitudes, such as the Mid-Alt operation at an altitude of 5 km and the MASCOT deployment operation at an altitude of about 50 m (Jaumann et al. 2019).

In this study, we used a high-definition shape model of 786,432 polygons (SFM 800k v20180804) derived from ONC observations, which was smaller than the TIR pixel scale; our previous studies used the model of 196,608 polygons (SFM 200k v20180804), which is the comparable size of the TIR pixel scale (Okada et al. 2020; Shimaki et al. 2020).

TIR images

TIR took thermal images of Ryugu as brightness temperature, which is represented as thermal emission from a black body in radiative equilibrium with sunlight (e.g., Hapke 2012). The observed data of TIR were converted from digital data to brightness temperature using a calibration database "HEAT" (Endo et al. 2017). The calibration table was constructed in prelaunch experiments (Okada et al. 2020; Arai et al. 2017). The observed data are released in JAXA/DARTS (Yamamoto et al. 2016) and NASA/PDS, which are raw digital images (Level 1 product) and brightness temperature images (Level 2 product).

Shape model of Ryugu

The surface terrain of Ryugu has been modeled by numerical shape models constructed from ONC images (Watanabe et al. 2019). The shape models were derived by a structure from motion (SfM) method (e.g., Szeliski 2010)

and a stereo photoclinometry (SPC) method (Gaskell et al. 2010). The 3M, 800k, and 200k shape models of Ryugu are composed of 3,145,728, 786,432, and 196,608 triangles; the sizes of the polygon triangles are tens centimeters, about 1 meter, and a few meters, respectively. We used the 800k model (SfM) in this study because the polygon size was small enough for TIR analysis and the SPICE kernel of this SFM model was compatible with TIR analysis.

SPICE kernels

NASA's numerical toolkit for the geometry system of the space mission called SPICE kernels (NASA/NAIF) for the Hayabusa2 mission has been released on the website of JAXA/DARTS. The SPICE kernels include the spacecraft information on trajectories derived from data of AOCS and LIDAR. The alignment information of TIR is included in a frame kernel (FK) of the SPICE kernel. The observation coordinate of TIR could be calculated by complementing data of ONC and LIDAR observation; TIR and ONC nominally took images alternately. However, the pointing coordinate of TIR was uncertain when observations with ONC and LIDAR were not performed.
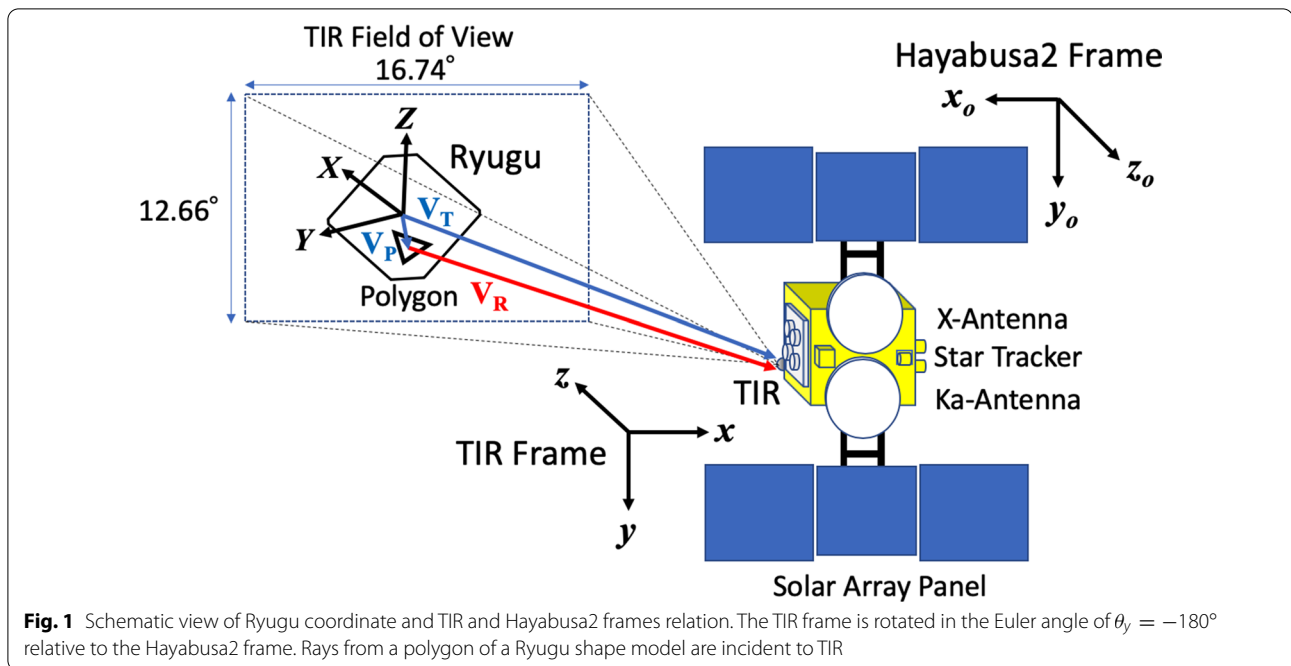
We analyzed data of early major observations (Box-A, Box-C, Mid-Alt, and Box-B) using version 03 of the SPICE kernel, released in March 2020. Version 03 kernels contain the improved trajectory of Hayabusa2 derived from LIDAR (Matsumoto et al. 2020) but do not include the relative position and attitude between Ryugu and Hayabusa2 derived from the shape model. The new version of the SPICE kernels for Hayabusa2 will be released in 2021 and includes a precise attitude of Hayabusa2 derived from the shape model, along with the results of this study.

Method: geometric correction

To fit positions observed by TIR to the coordinates of a shape model, rotating the TIR image frame using the SPICE toolkit (N0066) is performed. The temperatures of the observation images are represented by $T(i, j)$ in the image pixel coordinate, where i and j are the index of pixels ($i = 1 \sim 328$, $j = 1 \sim 248$), respectively. On the other hand, the observed brightness temperatures projected on polygons of a shape model are represented by $T(X, Y, Z)$ in the Cartesian coordinate of the Ryugu system (Fig. 1), where the positional vector of the polygon faces are denoted by $\mathbf{V}(X, Y, Z)$.

Projection from image to shape

The brightness temperature projection from a TIR image to a shape model of Ryugu is expressed as a coordinate transformation from the pixel coordinate to the Ryugu coordinate. We assume that the observed brightness

Arai *et al. Earth, Planets and Space* (2021) 73:115

Page 4 of 11

Fig. 1 Schematic view of Ryugu coordinate and TIR and Hayabusa2 frames relation. The TIR frame is rotated in the Euler angle of $\theta_y = -180°$ relative to the Hayabusa2 frame. Rays from a polygon of a Ryugu shape model are incident to TIR

temperature of a pixel value is the mean temperature of the observed region because the TIR pixel detects total radiation fluxes from a region of the Ryugu surface (e.g. ~5 m squares in Mid-Alt observation). The brightness temperature value of an image is directly converted to a shape model as $T(i,j) \rightarrow T(X,Y,Z)$. This transformation is represented by using the vector sum of positional vectors. A ray vector $\mathbf{V_R}$ from a polygon of the shape model of Ryugu to TIR is written as $\mathbf{V_R} = \mathbf{V_T} - \mathbf{V_P}$, where $\mathbf{V_P}$ and $\mathbf{V_T}$ are position vectors of the polygon and TIR, respectively (Fig. 1). The ray vector in the coordinated system of Ryugu $\mathbf{V_R}$ is transformed into that of the coordinate system of Hayabusa2 $\mathbf{v_R}$ using a coordinate conversion tool of the SPICE kernels, as $\mathbf{V_R} \rightarrow \mathbf{v_R}$.

A normalized boresight vector of TIR in the coordinated system of TIR is $(x, y, z) = (0, 0, 1)$. The frame of TIR is the coordinate system of Hayabusa2 that rotated the angle of $-180°$ in the y-axis (Fig. 1). The focal point length of the TIR is 42.2 mm, and thus the positional vector of the focal point is written as $\mathbf{v_F}(x, y, z) = (0, 0, 0.0422)$. The incident rays from polygons of the shape model to TIR intersect the image plane of TIR at the positional vector $\mathbf{v_I}$, where $\mathbf{v_I} = \mathbf{v_R} + \mathbf{v_F}$. The pixel size of the TIR sensor is 37 square μm, and thus the scalar value $|\mathbf{v_I}(x, y, z)|$ normalized by the pixel size is equivalent to the pixel coordinate (i, j).

Projection from shape to image

The projection temperature from a shape to an image is written as an inverse process of the image projection to

shape coordinate. However, this reprojection process is irreversible because it is not one-to-one correspondence as $T(X, Y, Z) \nrightarrow T(i, j)$. Here, the radiant flux F from the polygons to a pixel of the image as the sum of their radiations is calculated, using the Stefan-Boltzmann law and the scattering component of the solar ray, as follows:

$$F = \frac{1}{\pi} \sum_k \epsilon_k \sigma T_k^4 s_k \cos \phi_k + \text{scattering}, \tag{1}$$

where ϵ_k is the emissivity, σ is the Boltzmann constant, s_k is the area of the polygons, ϕ_k is the emission angle to the TIR direction, and k denotes the index of the polygon. The observation area for one pixel is written as the sum of the polygon areas, as follows:

$$S = \sum_k s_k \cos \phi_k. \tag{2}$$

We neglect the scattering component because the intensity of the radiation flux in the 8 to 12 μm wavelength range is more than two orders of magnitude smaller than that of the infrared radiation of a body around 300 K. We assume a constant emissivity for each polygon face. Thus, the reimaged temperature τ for a pixel is rewritten using Eqs. (1) and (2), as follows:

$$\tau \sim \left(\frac{\pi F}{\epsilon \sigma S} \right)^{\frac{1}{4}}. \tag{3}$$

Arai *et al. Earth, Planets and Space* (2021) 73:115

Page 5 of 11

Fitting alignment

The TIR frame $\mathbf{v}_T(x, y, z)$ is defined based on the Hayabusa2 frame $\mathbf{v}_H(x_o, y_o, z_o)$. The frame transformation is described using the Euler rotation, as follows:

$$\mathbf{v}_H = R_z R_y R_x \mathbf{v}_T, \tag{4}$$

where R_z, R_y, and R_x form the Euler rotation matrix in the right-handed coordinate system. The matrix R_z is the rotation of the TIR boresight vector, which has a bimodal path in the clockwise and the counterclockwise rotations. In this study, R_z is fixed as a unit matrix because this parameter is not effective in minimizing the converge value of the least squares fittings. Hence, Eq. (4) is written, as follows:

$$\begin{bmatrix} x_o \\ y_o \\ z_o \end{bmatrix} = \begin{bmatrix} \cos\theta_y & \sin\theta_y \sin\theta_x & -\sin\theta_y \cos\theta_x \\ 0 & \cos\theta_x & \sin\theta_x \\ \sin\theta_y & -\cos\theta_y \sin\theta_x & \cos\theta_y \cos\theta_x \end{bmatrix} \begin{bmatrix} x \\ y \\ z \end{bmatrix}, \tag{5}$$

where θ_x and θ_y are the Euler angles.

TIR observation points are determined by fitting the observation image to the projection image and onto the shape model of Ryugu. This adjustment is performed by minimizing the difference between the observed temperature image $T(i, j)$ and the reprojected temperature image from the Ryugu shape $T'(i, j)$ using the least squares fit, as follows:

$$\text{RSS} = \sum_{i,j} \left[T(i, j) - T'(i, j) \right]^2, \tag{6}$$

where RSS is a residual sum of squares in temperature. The free parameters of this fitting are the Euler angles of θ_y and θ_x in Eq. (5). The fitting is performed by using the algorithms of the Levenberg-Marquardt and Simplex fitting method (e.g. Press et al. 2007). The fitting converged value of RSS is ideally zero.

Figure 2 shows an example of the geometric correction procedure for an image (Mid-Alt observation, 23:07), which is the observed image projected onto the shape model and reprojected onto images. The best-fit Euler angles as free parameters of θ_y and θ_x are determined by reducing the residuals of the observed image and the reproduced image.

Results

The geometric correction was performed for all observed images of TIR in the early major observations. Table 1 shows the best-fit alignment values (Euler angle), along with the observation configuration for each observation,
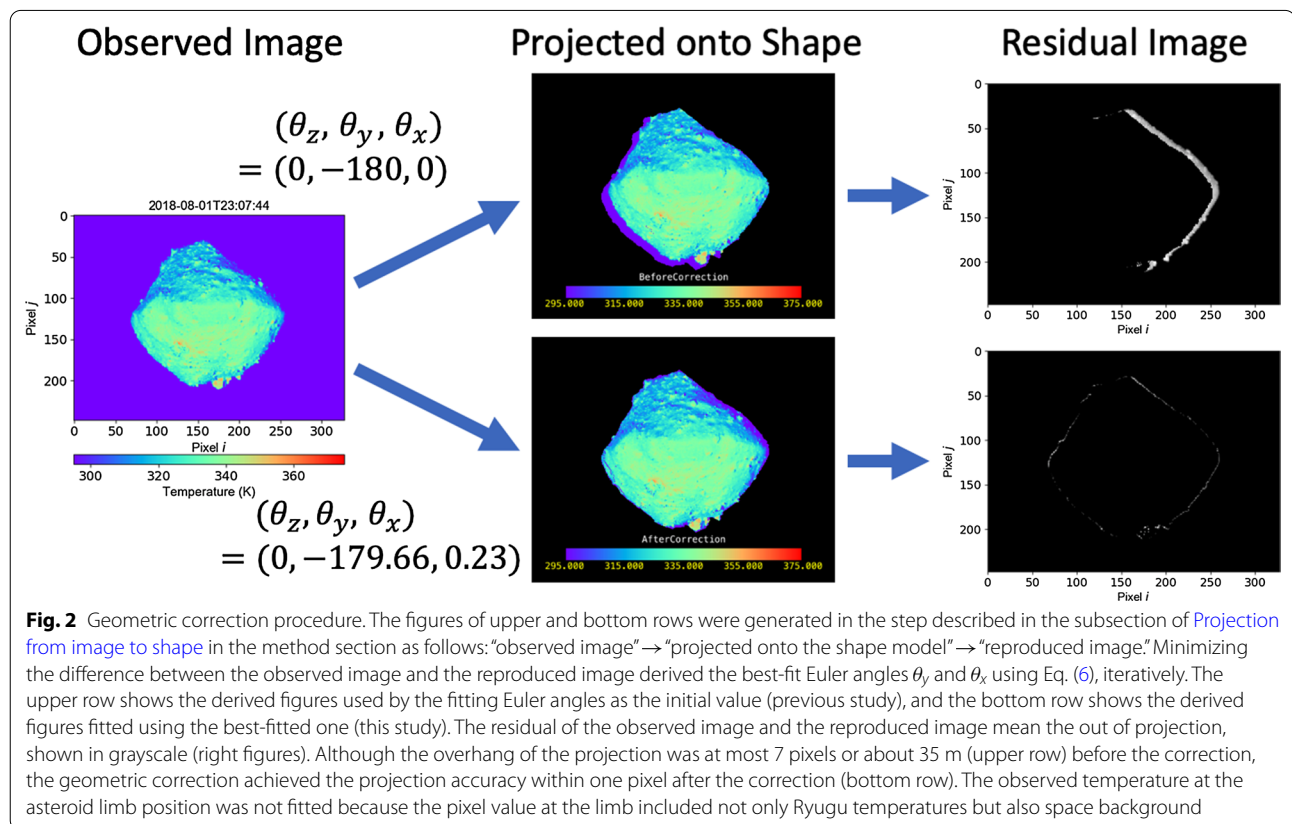

Fig. 2 Geometric correction procedure. The figures of upper and bottom rows were generated in the step described in the subsection of Projection from image to shape in the method section as follows: "observed image" → "projected onto the shape model" → "reproduced image." Minimizing the difference between the observed image and the reproduced image derived the best-fit Euler angles θ_y and θ_x using Eq. (6), iteratively. The upper row shows the derived figures used by the fitting Euler angles as the initial value (previous study), and the bottom row shows the derived figures fitted using the best-fitted one (this study). The residual of the observed image and the reproduced image mean the out of projection, shown in grayscale (right figures). Although the overhang of the projection was at most 7 pixels or about 35 m (upper row) before the correction, the geometric correction achieved the projection accuracy within one pixel after the correction (bottom row). The observed temperature at the asteroid limb position was not fitted because the pixel value at the limb included not only Ryugu temperatures but also space background
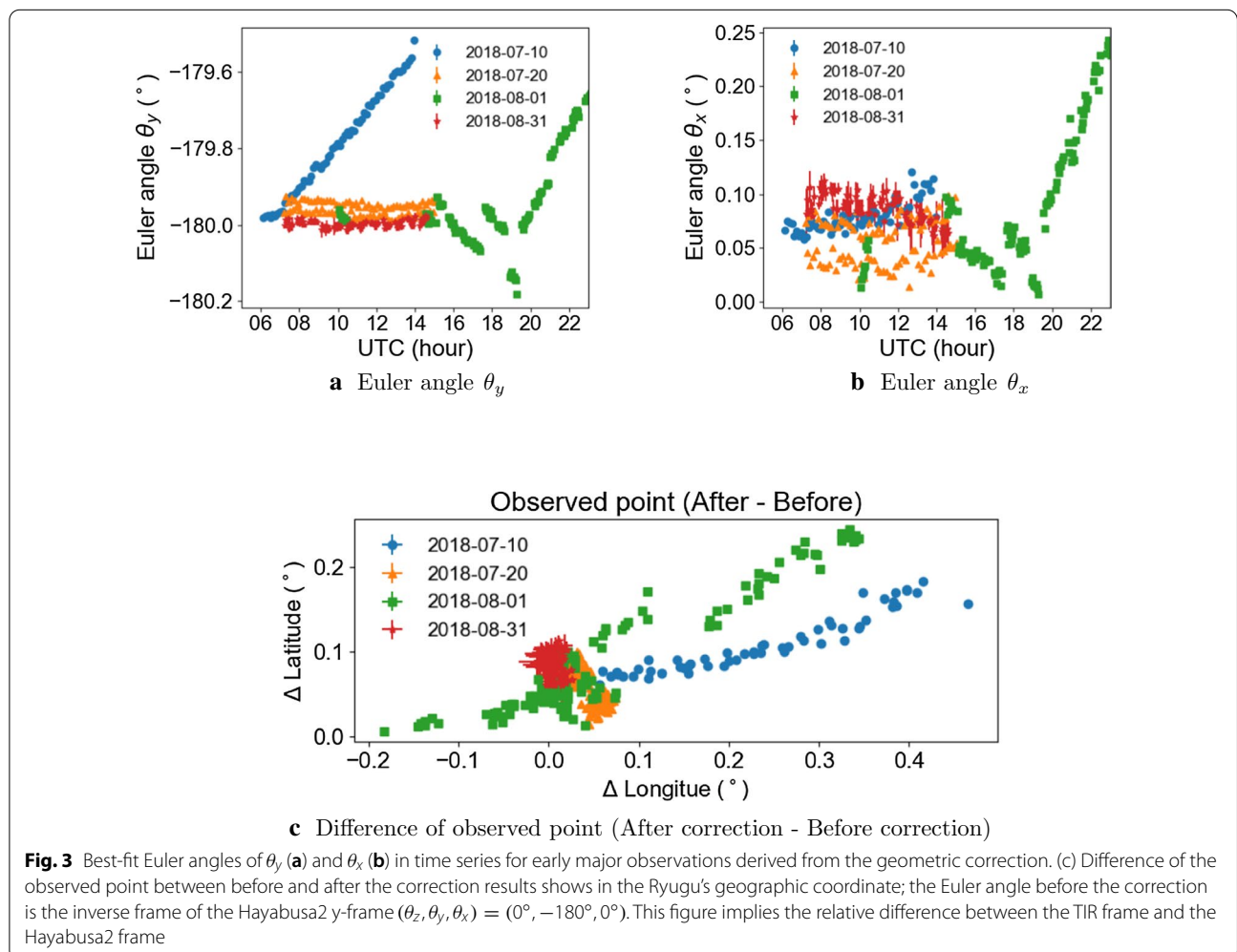
Table 1 Observation configuration and mean values of the best-fit Euler angles

Observation (-)	Sun distance (AU)	Phase angle (°)	SC Latitude (°)	Altitude (km)	Image (-)	Euler $\bar{\theta}_Y$ (°)	Euler $\bar{\theta}_X$ (°)
Box-A	1.005	18.57	−4.33	19.58	64	−179.78	0.08
(2018-07-10)	–	± 0.07	± 0.01	± 0.05	–	± 0.13	± 0.01
Box-C	1.028	18.45	−4.93	6.59	96	−179.95	0.06
(2018-07-20)	–	± 0.12	± 0.08	± 0.08	–	± 0.01	± 0.01
Mid-Alt	1.060	18.98	−5.37	5.28	120	−179.93	0.09
(2018-08-01)	–	± 0.17	± 0.08	± 0.33	–	± 0.13	± 0.07
Box-B	1.148	40.10	−1.66	21.41	96	−180.00	0.08
(2018-08-31)	–	± 0.10	± 0.01	± 0.04	–	± 0.01	± 0.01

such as the solar distance, the solar phase angle, the sub-spacecraft latitude, the spacecraft altitude, and the number of observed images. The error of the Euler angles is the standard deviation of each best-fit value.

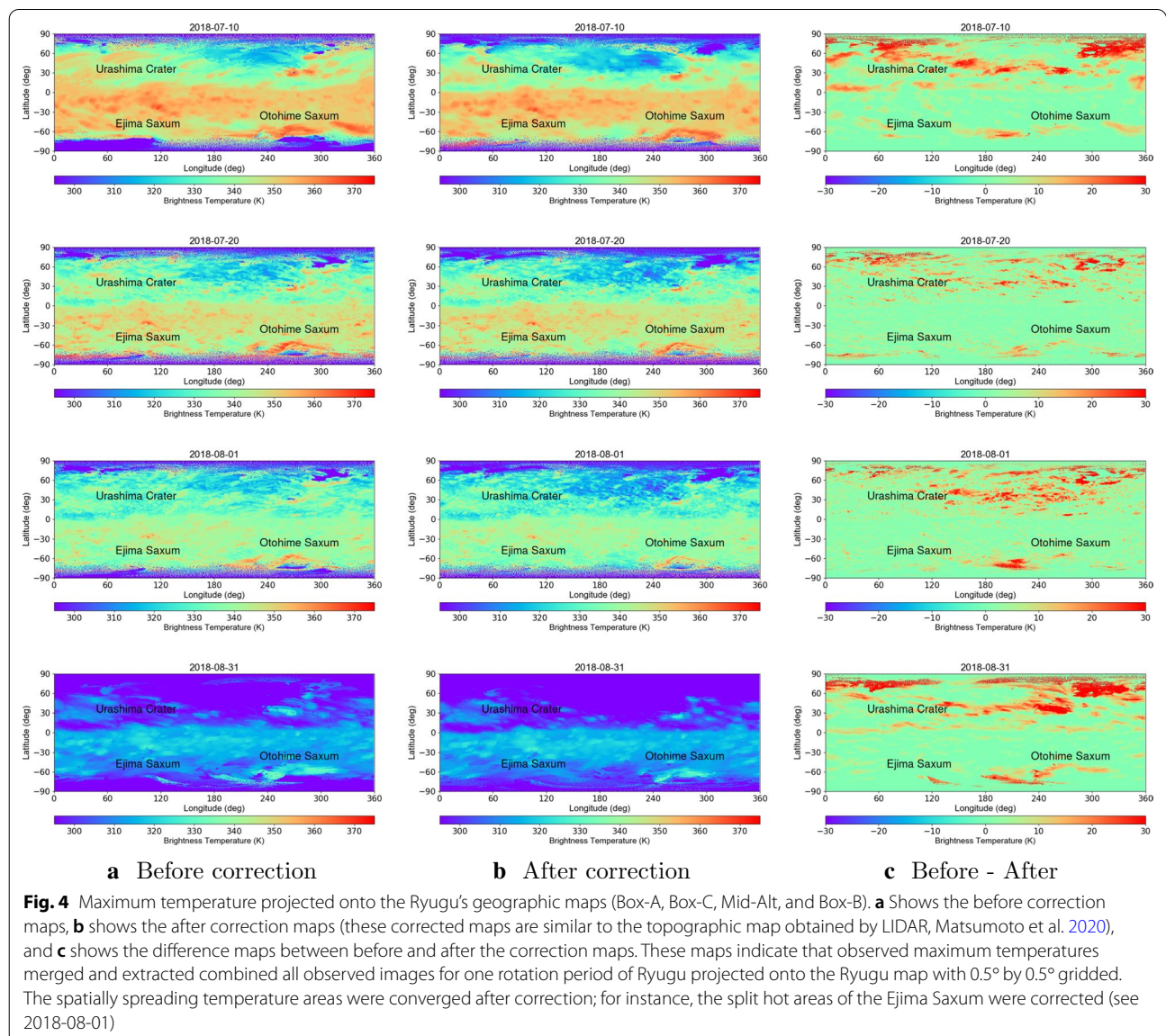Figure 3a and b show the best-fit Euler angles of θ_y and θ_x in time series for all images of each observation. The resulting Euler angles were increased (decreased) along with Hayabusa2 attitude while the Ryugu-pointing was not performed, such as Box-A (2018-07-10) and Mid-Alt (2018-08-01) observations. On the other hand, the Euler angles were stable in the observations of Box-C (2018-07-20) and Box-B (2018-08-31) because the Ryugu-pointing

a Euler angle θ_y

b Euler angle θ_x

c Difference of observed point (After correction - Before correction)

Fig. 3 Best-fit Euler angles of θ_y (**a**) and θ_x (**b**) in time series for early major observations derived from the geometric correction. (c) Difference of the observed point between before and after the correction results shows in the Ryugu's geographic coordinate; the Euler angle before the correction is the inverse frame of the Hayabusa2 y-frame $(\theta_z, \theta_y, \theta_x) = (0°, -180°, 0°)$. This figure implies the relative difference between the TIR frame and the Hayabusa2 frame

Arai *et al. Earth, Planets and Space*   (2021) 73:115

Page 7 of 11

was continuously performed. Ryugu scanning observations were carried out in Box-C to measure the sensitivity of the TIR's angle of view, and thus the Euler angles had the bimodal feature in Box-C. Figure 3c shows the difference of the TIR observed point (footprint) between before and after the correction results in the Ryugu's geographic coordinate; the alignment value before the correction was the inverse frame of the Hayabusa2 y-frame $(\theta_z, \theta_y, \theta_x) = (0°, -180°, 0°)$. Thus, this figure implies the relative difference between the TIR frame and the Hayabusa2 frame. Although large differences were seen in the resulting values of Box-A and Mid-Alt observations, caused by the attitude changes of Hayabusa2, that of Box-B was stable. Therefore, we believe that the resulting

value of Box-B represented the accurate alignment value of TIR. We concluded that the alignment value of TIR is $(0.00°, -180.00°, 0.08°)$ and release this value as a new FK of the Hayabusa2 SPICE kernels in 2021.

Figure 4 shows the maximum temperature maps projected onto Ryugu maps with 0.5° by 0.5° gridded before and after the geometric correction (Box-A, Box-C, Mid-Alt, and Box-B). These maximum temperatures were merged and extracted, combined with all observed images of the Ryugu's one rotation period obtained with the observed time interval of 76 s. We can see that the temperature maps spatially spreading areas are converged in the map of 0.5° gridded after the correction; for instance, the temperature of the splitting area at the

a Before correction   **b** After correction   **c** Before - After

Fig. 4 Maximum temperature projected onto the Ryugu's geographic maps (Box-A, Box-C, Mid-Alt, and Box-B). **a** Shows the before correction maps, **b** shows the after correction maps (these corrected maps are similar to the topographic map obtained by LIDAR, Matsumoto et al. 2020), and **c** shows the difference maps between before and after the correction maps. These maps indicate that observed maximum temperatures merged and extracted combined all observed images for one rotation period of Ryugu projected onto the Ryugu map with 0.5° by 0.5° gridded. The spatially spreading temperature areas were converged after correction; for instance, the split hot areas of the Ejima Saxum were corrected (see 2018-08-01)

Arai *et al. Earth, Planets and Space*   (2021) 73:115

Page 8 of 11

Ejima Saxum before the correction (left figure of 2018-08-01) is about 20 K larger than the surrounding temperature, but the area is successfully converged after the correction (middle figure of 2018-08-01). This correction is important for thermal inertia estimation because the maximum temperature of the temperature profile affects the derived value of thermal inertia. The geometric correction succeeded in detailed map construction with the low altitude observations (Box-C and Mid-Alt), and the correction was also effective for observed data at a high altitude observation of 20 km (Box-A and Box-B) because the spreading temperature areas were more converged.

Discussion

The geometric correction carried out the temperature map construction within the accuracy of the pixel scale of TIR; the spatially spreading temperature areas were converged in 0.5° by 0.5° gridded after the correction. Here, we discuss the reproducibility of the observed temperature projected onto the shape model and map, compared with numerical simulation results, such as the specific region of Ejima Saxum and Urashima crater.

Figure 5a shows an example of one image projected on a map using the shape model of Ryugu (SFM 800k v20180804). Figure 5b and c show examples of the temperature profiles of the hot areas of the Ejima Saxum and Urashima crater in time series, derived from the temperature map projected onto a Ryugu map using 31 observed images with 0.5° by 0.5° gridded. The profile before and after the correction varied in the Ejima Saxum as a characteristic area, but the profile was not significantly changed in the Urashima crater as a smooth area (top Figures of 5b and c). Therefore, the geometric correction is important for the detailed estimation of the temperature profile in topographically characteristic areas, such as the Ejima Saxum; the difference of the profile will cause the error of thermal inertia estimation at least ~ 50 $Jm^{-2}s^{-0.5}K^{-1}$.

The observed temperature profiles of the Ejima Saxum and the Urashima crater and the simulated temperature profiles derived from TPM-1 (Takita et al. 2017) in the thermal inertia steps of 100 $Jm^{-2}s^{-0.5}K^{-1}$ are shown in bottom Figures of 5b and c. The thermal inertia of the Ejima Saxum was estimated to be 300 $Jm^{-2}s^{-0.5}K^{-1}$ except the temperature profile at dawn time ($\sim$14:30) and dusk time ($\sim$17:00). On the other hand, the thermal inertia of the Urashima crater was approximately 200 to 400 $Jm^{-2}s^{-0.5}K^{-1}$. This difference between the observed profile and the simulated profiles of the Urashima crater was also probably caused by the surface roughness. These results indicate that the brightness temperatures of observed areas larger than a TIR pixel scale, such as characteristic areas, are dependent on large-scale surface topography that can be reproduced by TPM-1. On the other hand, the brightness temperatures of observed areas smaller than a TIR pixel scale, such as smooth areas, are dependent on small-scale roughness is required to be reproduced by TPM-2 (Shimaki et al. 2020).

Figure 6 shows the observed image and the anticipated image reproduced by TPM-1 using the shape model (SFM 800k v20180804). The hot regions are found at the bottom of Ejima Saxum and Otohime Saxum in both of the observed and the anticipated images (see the closed-up images of ONC, Figs. 1(B) and 2(A) Sugita et al. 2019). The simulation parameters of TPM-1 were assumed to be an emissivity of 1.0, an albedo of 0.045 (Sugita et al. 2019), and a thermal inertia of 350 Jm^{-2} $s^{-0.5}K^{-1}$. The observed image (Fig. 6a) is similar to the anticipated image (Fig. 6b) at the hot areas. This model involves the effect of secondary radiation, and thus this result implies that the secondary radiations between surrounding terrains generate the hot areas. Although the thermal inertia at the bottom of Ejima Saxum resulted in the thermal inertia profile of approximately 300 $Jm^{-2}s^{-0.5}$ K^{-1} (Fig. 5b), this anticipated image was reproduced well by using the value of 350 $Jm^{-2}s^{-0.5}K^{-1}$. Also, the globally homogeneous temperature of the observed image is not reproduced by TPM-1. These differences are probably caused by surface roughness because the surface roughness can flatten the whole temperature of the surface.

We conclude that the development of a thermophysical model, including a hybrid model that implements topography (TPM-1) and small-scale surface roughness (TPM-2), is required.

Summaries

The accurate alignment value of TIR was determined, $(\theta_z, \theta_y, \theta_x) = (0.00°, -180.00°, 0.08°)$. This positioning accuracy of TIR was improved equivalent to a pixel scale ($\sim$ 5 m at an altitude of 5 km observation). The resulting alignment value is released as the new version FK of the Hayabusa2 SPICE kernels. The higher degree products of TIR constructed by using the geometric correction are also released on the website of JAXA/DARTS and NASA/PDS in 2021.

The observed temperature maps—which were projected onto the Ryugu map spatially spreading areas are improved by the geometric correction and constructed with high-resolved 0.5° by 0.5° gridded.

The thermal inertia estimation of a characteristic area was succeeded in case that the surface topographic features larger than the TIR pixel scale, which the temperature profile can be reproduced by TPM-1. In contrast, the thermal inertia estimation of the smooth area was inaccurate. This phenomenon was probably caused by surface roughness much smaller than the TIR pixel scale;
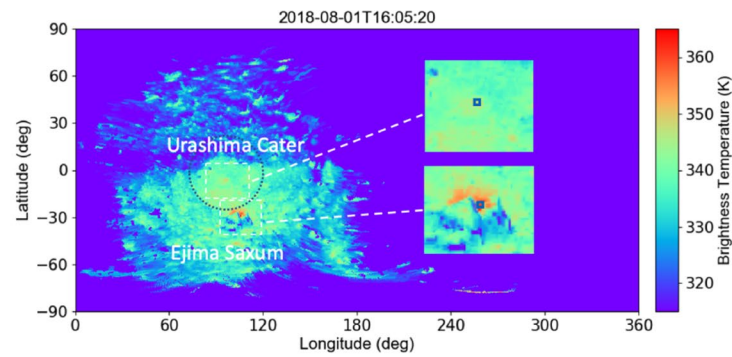
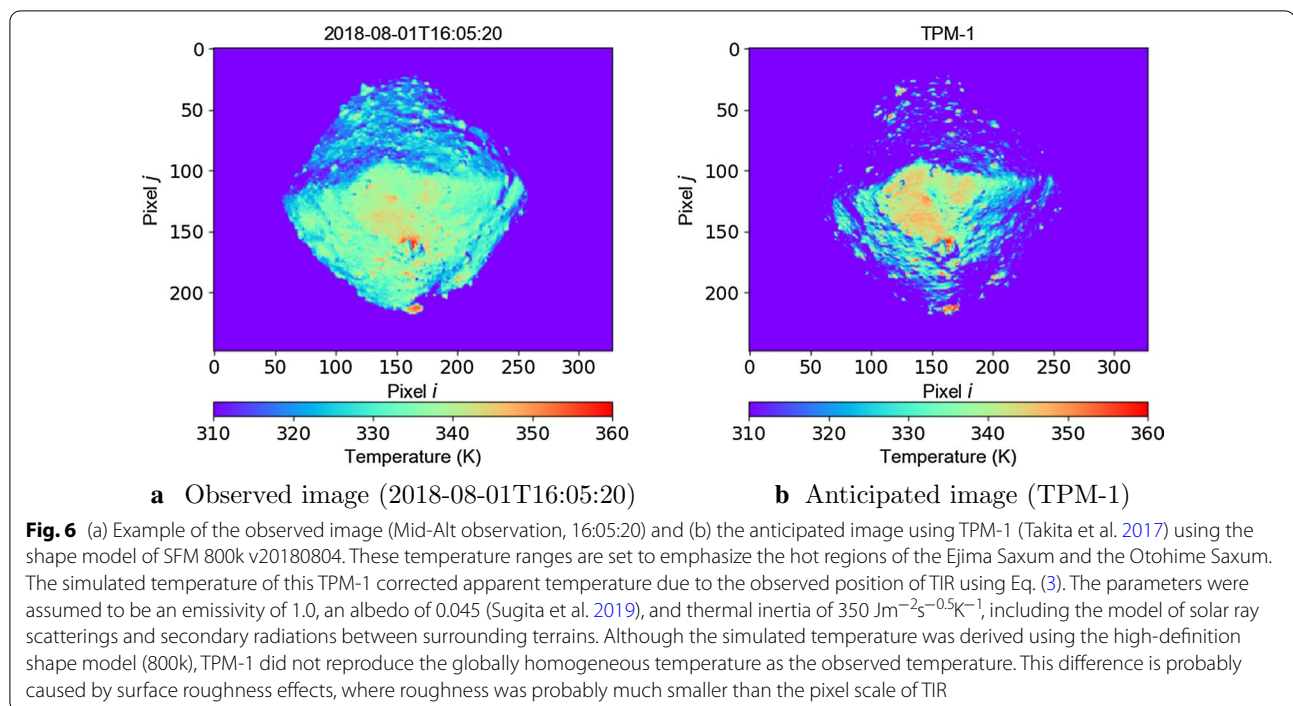**a** Projected map of one TIR image (Mid-Alt observation, 16:05:20)
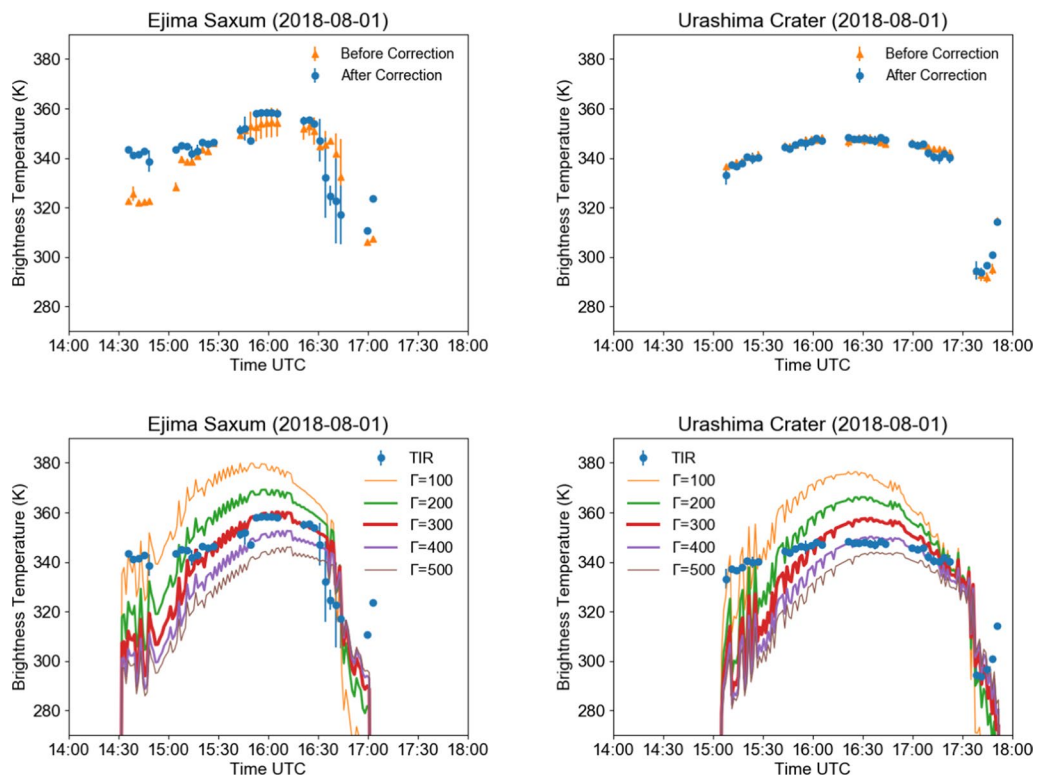
b Hot area of Ejima Saxum   **c** Hot area of Urashima crater

Fig. 5 **a** Shows an example of one image projected on the map using the shape model of Ryugu (SFM 800k v20180804) in the map of 0.5° by 0.5° gridded. **b**, **c** Show the temperature profiles at the hot area of the Ejima Saxum (Lat: −28.0°, Lon: 106.0°) and the Urashima crater (Lat: −6.5°, Lon: 96.5°), which were derived from 31 images extracted from the hot areas as shown in the square area of **a**. The orange and blue points in the top figures of **b** and **c** denote the observed temperature profiles before and after the geometric correction, respectively. The temperature profile after the correction (blue points) of the Ejima Saxum is matched to the simulated temperature profile derived from TPM-1 (Takita et al. 2017), assuming the thermal inertia value of 300 Jm^{-2}s$^{-0.5}$K^{-1} (bottom figure of b), but that of the Urashima crater is not matched to the simulation (bottom figure of c)

such temperature profiles can be reproduced by TPM-2. We conclude that the development of a thermophysical model, including a hybrid model that implements topography and small-scale surface roughness, is required to reveal the actual surface state of Ryugu.

Arai *et al. Earth, Planets and Space* (2021) 73:115

Page 10 of 11

Fig. 6 (a) Example of the observed image (Mid-Alt observation, 16:05:20) and (b) the anticipated image using TPM-1 (Takita et al. 2017) using the shape model of SFM 800k v20180804. These temperature ranges are set to emphasize the hot regions of the Ejima Saxum and the Otohime Saxum. The simulated temperature of this TPM-1 corrected apparent temperature due to the observed position of TIR using Eq. (3). The parameters were assumed to be an emissivity of 1.0, an albedo of 0.045 (Sugita et al. 2019), and thermal inertia of 350 $Jm^{-2}s^{-0.5}K^{-1}$, including the model of solar ray scatterings and secondary radiations between surrounding terrains. Although the simulated temperature was derived using the high-definition shape model (800k), TPM-1 did not reproduce the globally homogeneous temperature as the observed temperature. This difference is probably caused by surface roughness effects, where roughness was probably much smaller than the pixel scale of TIR

Abbreviations
AOCS:: Attitude and Orbit Control System; DARTS:: Data Archive and Transmission System; FK:: Frame Kernel; JAXA:: Japan Aerospace Exploration Agency; LIDAR:: Light detection and ranging; MASCOT:: Mobile Asteroid Surface Scout; Mid-Alt:: Middle Altitude; NAIF:: Navigation and Ancillary Information Facility; NASA:: National Aeronautics and Space Administration; NIRS3:: Near infrared spectrometer; ONC:: Optical navigation camera; RSS:: Residual sum of squares; SC:: Spacecraft; SfM:: Structure from motion; SPC:: Stereo photoclinometry; SPICE:: Spacecraft Planet Instrument C-matrix Events; TIR:: Thermal infrared imager; TPM:: Thermophysical model; UTC:: Coordinated Universal Time.

Authors' contributions
TA: Preparation of the manuscript, Methodology, and Data analysis; TO: Methodology, and Administration of TIR science team; ST, TF: Administration of TIR science team; HD: Software development; TK, YS, HS, TS: Methodology; NS, JT: Data analysis; NH: Software development; YY: Science operation of the spacecraft. All authors read and approved the final manuscript.

Availability of data and materials
The original data of this study are available and downloadable on the following website:
TIR data: https://www.darts.isas.jaxa.jp/pub/hayabusa2/tir_bundle/browse/
SPICE kernels: https://www.darts.isas.jaxa.jp/pub/hayabusa2/spice_bundle/document/spiceds_v001.html.

Declarations

Competing interests
The authors declare that they have no competing interests.

Author details
[1]Division of Systems and Information Engineering, Ashikaga University, Ashikaga 326-8558, Japan. [2]Present Address: Department of Systems Life Engineering, Maebashi Institute of Technology, Maebashi 371-0816, Japan. [3]Institute of Space and Astronautical Science, Japan Aerospace Exploration Agency (JAXA), Sagamihara 252-5210, Japan. [4]The University of Tokyo, Tokyo 113-0033, Japan. [5]The Graduated University for Advanced Studies, SOKENDAI, Hayama 240-0193, Japan. [6]Rikkyo University, Tokyo, Japan. [7]The University of Aizu, Aizu-Wakamatsu 965-8580, Japan. [8]National Institute of Advanced Industrial Science and Technology, Tokyo, Japan. [9]Planetary Exploration Research Center, Chiba Institute of Technology, Narashino 275-0016, Japan. [10]Hokkaido University of Education, Sapporo 002-8501, Japan. [11]Hokkaido Kitami Hokuto High School, Kitami 090-0035, Japan.

References
Arai T et al (2017) Thermal imaging performance of TIR onboard the Hayabusa2 Spacecraft. Space Sci Rev 208:239–254. https://doi.org/10.1007/s11214-017-0353-9

Binzel RP et al (2004) Observed spectral properties of near-earth objects: results for population distribution, source regions, and space weathering processes. Icarus 170(2):259–294. https://doi.org/10.1016/j.icarus.2004.04.004

Arai *et al. Earth, Planets and Space*   (2021) 73:115

Page 11 of 11

Bottke WF Jr et al (2006) The Yarkovsky and YORP effects: implications for asteroid dynamics. Annu Rev Earth Planet Sci. 34:157–91

Endo K et al (2017) HEAT: Image and database browser for the thermal imager on Hayabusa2. IEEE Aerospace Conference 1–10. https://doi.org/10.1109/AERO.2017.7943827

Gaskell RW et al (2010) Characterizing and navigating small bodies with imaging data. Meteor Planet Sci. 43(6):1049–1061. https://doi.org/10.1111/j.1945-5100.2008.tb00692.x

Grott et al (2020) Macroporosity and grain density of rubble pile asteroid (162173) Ryugu. J Geophys Res. https://doi.org/10.1029/2020JE006519

Groussin O et al (2007) Surface temperature of the nucleus of Comet 9P/Tempel 1. Icarus 187(1):16–25. https://doi.org/10.1016/j.icarus.2006.08.030

Hapke (2012) Thermal emission and emittance spectroscopy, Theory of Reflectance and Emittance Spectroscopy. Cambridge University Press 412–439. https://doi.org/10.1017/CBO9781139025683

Jaumann R et al (2019) Images from the surface of asteroid Ryugu show rocks similar to carbonaceous chondrite meteorites. Science 365:817–820. https://doi.org/10.1126/science.aaw8627

Kitazato K et al (2019) The surface composition of asteroid 162173 Ryugu from Hayabusa2 near-infrared spectroscopy. Science 364(6437):272–275. https://doi.org/10.1126/science.aav7432

Matsumoto K et al (2020) Improving Hayabusa2 trajectory by combining LIDAR data and a shape model. Icarus. https://doi.org/10.1016/j.icarus.2019.113574

Müller TG et al (2017) Hayabusa-2 mission target asteroid 162173 Ryugu (1999 JU3): searching for the object's spin-axis orientation. Astron Astrophys 599:A103. https://doi.org/10.1051/0004-6361/201629134

Okada T et al (2017) Thermal infrared imaging experiments of C-type asteroid 162173 Ryugu on Hayabusa2. Space Sci Rev 208:255–286. https://doi.org/10.1007/s11214-016-0286-8

Okada T et al (2018) Earth and moon observations by thermal infrared imager on Hayabusa2 and the application to detectability of asteroid 162173 Ryugu. Planet Space Sci 158:46–52. https://doi.org/10.1016/j.pss.2018.05.007

Okada T et al (2020) Highly porous nature of a primitive asteroid revealed by thermal imaging. Nature 579:518–522. https://doi.org/10.1038/s41586-020-2102-6

Press WH et al (2007) Modeling of data, numerical recipes, 3rd edn. Cambridge University Press, Cambridge, pp 773–839

Shimaki Y et al (2020) Thermophysical properties of the surface of asteroid 162173 Ryugu: infrared observations and thermal inertia mapping. Icarus. https://doi.org/10.1016/j.icarus.2020.113835

Sugita S et al (2019) The geomorphology, color, and thermal properties of Ryugu: Implications for parent-body processes. Science. https://doi.org/10.1126/science.aaw0422

Szeliski R (2010) Computer vision: algorithms and applications. Berlin, Springer

Takita J et al (2017) Feasibility and accuracy of thermophysical estimation of asteroid 162173 Ryugu (1999 JU$_3$) from the Hayabusa2 thermal infrared imager. Space Sci Rev 208:287–315. https://doi.org/10.1007/s11214-017-0336-x

Tsuda Y et al (2013) System design of the Hayabusa 2 - asteroid sample return mission to 1999 JU$_3$. Acta Astronaut 91:356–362

Watanabe S et al (2019) Hayabusa2 arrives at the carbonaceous asteroid 162173 Ryugu - a spinning-top-shaped rubble pile. Science 364(6437):268–272. https://doi.org/10.1126/science.aav8032

Yamamoto Y et al (2016) Scientific data archives in Hayabusa2 mission. Trans JSASS Aerospace Tech Japan 14:151–154. https://doi.org/10.2322/tastj.14.Pk_151

Publisher's Note